ACS APPLIED MATERIALS & INTERFACES

Research Article

www.acsami.org

Efficient Photoelectrochemical Water Splitting over Anodized *p*-Type NiO Porous Films

Chenyan Hu, Kenneth Chu, Yihua Zhao, and Wey Yang Teoh*

Clean Energy and Nanotechnology (CLEAN) Laboratory, School of Energy and Environment, City University of Hong Kong, Kowloon, Hong Kong S.A.R.

Supporting Information

ABSTRACT: NiO photocathodes were fabricated by alkaline etching-anodizing nickel foil in an organic-based electrolyte. The resulting films have a highly macroporous surface structure due to rapid dissolution of the oxide layer as it is formed during the anodization process. We are able to control the films' surface structures by varying the anodization duration and voltage. With an onset potential of +0.53 V versus the reversible hydrogen electrode (RHE), the photocurrent efficiency of the NiO electrodes showed dependencies on their surface roughness factor, which determines the extent of semiconductor-electrolyte interface and the associated quality of the NiO surface sites. A maximum incident photon-to-current conversion efficiency ($IPCE_{max}$) of 22% was obtained from NiO film with a roughness factor of 8.4. Adding an Al_2O_3 blocking layer minimizes surface charge recombination on the NiO and hence increased the $IPCE_{max}$ to 28%. The NiO/Al_2O_3 films were extremely stable during photoelectrochemical water splitting tests lasting up to 20 h, continuously producing hydrogen and oxygen in the stoichiometric 2:1 ratio. The NiO/Al_2O_3 and NiO films fabricated using the alkaline anodization process produced 12 and 6 times as much hydrogen, respectively, as those fabricated using commercial NiO nanoparticles.

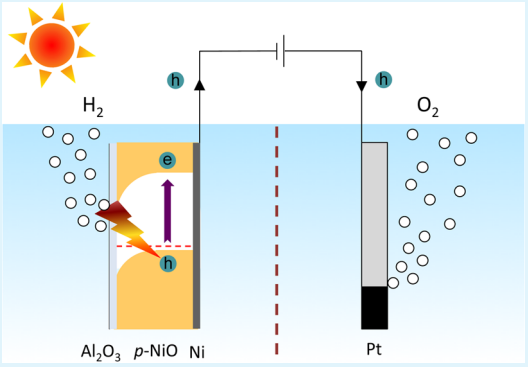

KEYWORDS: *nickel oxide, anodization, holes transport, hydrogen, water splitting*

1. INTRODUCTION

Metal oxide semiconductors have been the central to many robust and low-cost solar energy-related applications, including excitonic solar cells,[1] photoelectrochemical water splitting,[2] and photocharge storage.[3] To date, a series of *n*-type metal oxides such as titanium dioxide (TiO_2), zinc oxide (ZnO), bismuth vanadate ($BiVO_4$), hematite (α-Fe_2O_3), and tungsten trioxide (WO_3) have dominated much of the literature in these areas[4−8] because these films are chemically and thermally stable, easy to process, and naturally abundant. The photoelectrochemical (PEC) properties and charge transport behavior of these materials is now reasonably well-understood.[9,10] Recently, *p*-type oxide semiconductors have become a more active area of research, as paring *p*-type oxide cathodes with *n*-type oxide anodes will improve the performance and reduce the cost of solar harvesting systems.

Nickel oxide (NiO) and cuprous oxide (Cu_2O) are among the forefront *p*-type oxide semiconductors of interests.[11,12] More complex constructs such as $CuFeO_2$,[13] Rh-doped $SrTiO_3$,[14] Cr-doped TiO_2[15] and $La_5Ti_2CuS_5O_7$[16] have emerged more recently, some only exhibiting the *p*-type characteristics when subjected to sub-bandgap or extrinsic excitation. The hope is that robust and efficient *p*-type oxide semiconductors will be able to replace the platinum and gold counter electrodes used in conventional PEC systems while at the same time improving their efficiency by acting as a photocathode and thus contributing to the generated photocurrent. This concept was initially demonstrated by Bach and co-workers, who reported a photovoltaic solar efficiency of 2.42% for a tandem cell using a dye-sensitized NiO photocathode.[17] The work triggered the current research into *p*-type semiconductor electrodes for PEC applications.[18]

The biggest limitation of tandem PEC systems lies in the design of the photocathodes, which are characterized by relatively low quantum efficiencies. This is particularly true when using commercial NiO, which has not been designed for photoharvesting applications. Only limited work has been done on the parametric syntheses of *p*-type semiconductors and further characterization of their PEC properties.[19,20] In particular, NiO is a favored photocathode given its resistance to photocorrosion, even when used in iodide/triiodide redox electrolytes.[21]

In this study, we will describe a new method for the synthesis of porous NiO photocathodes by etching-anodization. Etching-anodization, or simply anodization, has become a mainstream technique for the fabrication of highly efficient electrodes over large, mechanically flexible substrates of any shape. A large number of these electrodes, mainly *n*-type TiO_2, Fe_2O_3, Nb_2O_5,

Received: May 20, 2014
Accepted: October 17, 2014
Published: October 17, 2014

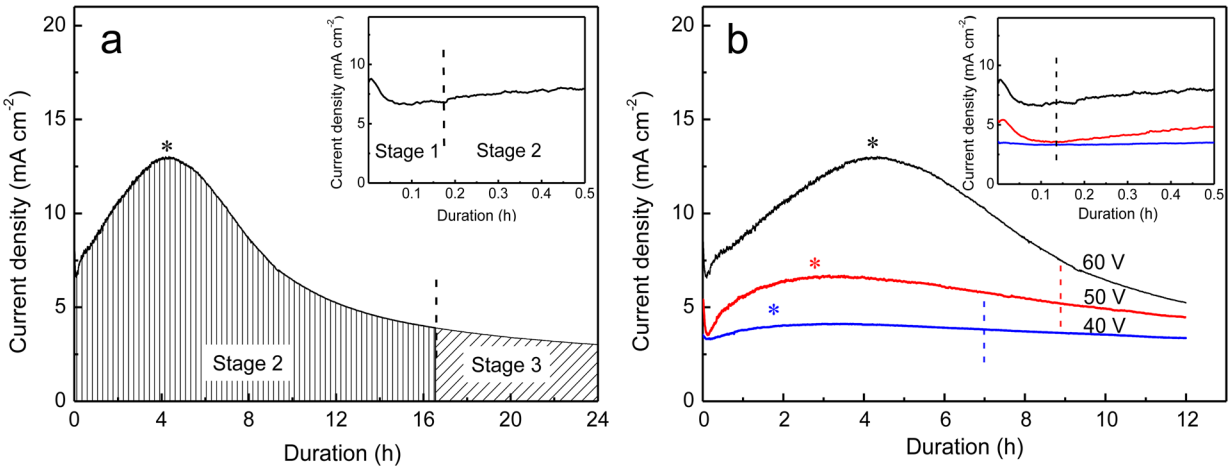

Figure 1. Transient currents during anodization of nickel foils (a) at 60 V for 24 h and (b) at different voltages for 12 h. The electrolyte was 0.5 wt % KOH, 5 wt % H_2O, and 94.5 wt % glycerol. The insets show the transient currents during the initial 0.5 h of anodization in panels a and b, while the asterisks (*) mark the maximum current densities.

and Ta_2O_5,[22−25] have been synthesized from the anodization in fluoridic or strongly acidic electrolytes. However, during our experimental screening leading to the current work, we found that NiO films could not be formed using standard anodization methods because the dissolution rate of NiO in acidic and fluoridic electrolytes was much faster than the growth rate of NiO itself. This is not the case when using an alkaline electrolyte, however, and it is this alkaline anodization technique that we shall be reporting on here. We will also discuss the characterization of the relationship between the physiochemical and charge transport behavior of the anodized NiO photocathodes and their superior performance in the *p*-type photoelectrochemical water splitting compared to electrodes fabricated from commercial NiO nanoparticles.

2. EXPERIMENTAL SECTION

2.1. Fabrication of NiO Electrodes. As-purchased nickel foil (99.9%, 0.15 mm thickness, BDH) was cleaned by successive sonication in Milli-Q water, ethanol, and acetone for 20 min each and dried under flowing N_2. The cleaned Ni foil was anodized in a two-electrode electrochemical cell at 40, 50, or 60 V using platinum ring as the counter electrode. Prior to use, electrolyte containing 0.5 wt % potassium hydroxide (KOH, >85%, Fluka), 5 wt % Milli-Q water, and 94.5 wt % glycerol (>99%, Aldrich) was aged for 20 min at the target anodization voltage. The transient anodic current was recorded on an online digital multimeter (Tektronix, DMM4020). The anodized Ni samples were rinsed and sonicated in Milli-Q water for 10 min to remove the residual electrolyte and dried under flowing N_2, followed by thermal annealing in a muffle furnace (Thermo). A thin Al_2O_3 layer was deposited on the annealed NiO film by immersing in 0.2 M aluminum trisec-butoxide (99.99%, Aldrich) in 2-propanol in a sealed Schott bottle.[26] The solution preparation and NiO immersion were carried out in a N_2 atmosphere glovebox. The sealed bottle containing NiO film was incubated in a 60 °C oven for 30 min. Upon cooling to room temperature, NiO film was retrieved, rinsed with 2-propanol, and calcined at 450 °C (ramping 5 °C min^{-1}) for 1 h.

Commercial NiO nanoparticles (99.8%, Aldrich) were dispersed in absolute ethanol (>99.5%, Aldrich) at 2 mg L^{-1} by sonication for 1 h and dropcast onto fluorine-doped tin oxide glass (FTO, Nippon Special Glass, 7 Ω/square) within an area of 5 cm^2. Dropcast was carried out stepwise with 0.5 mL suspension each time. Prior to use, the FTO glass was successively cleaned by sonication in water, ethanol, and acetone for 20 min each. The dropcast substrates were calcined at 400 °C (ramping 5 °C min^{-1}) for 1 h in a muffle furnace.

2.2. Physicochemical and Photoelectrochemical Characterization. Binding energies were measured by X-ray photoelectron spectroscopy (XPS) on PHI-5802 using Al Kα as the radiation source and referenced to C 1s peak at 284.6 eV. The crystalline structure of the samples was characterized by X-ray Diffraction (XRD; Philips X'Pert MPD) using Cu Kα irradiation source operating at 40 kV and 40 mA. The morphology of anodized Ni samples was imaged by SEM (JEOL, JSM 6300) and field emission-scanning electron microscopy (FESEM; JEOL JSM 7001F), equipped with electron diffractive X-ray (EDX) for elemental analysis. The topology of the electrodes was measured in tapping mode by atomic force microscopy (AFM) on Veeco Nano Scope V. The Fourier transform infrared spectroscopy (FTIR) spectra of the electrodes were measured by attenuated total reflectance (ATR) mode on Shimadzu IRAffinity-1S spectrophotometer. To assess the surface roughness, we immersed the NiO film in 1.5 mM aqueous methyl orange (MO) solution for 30 min, followed by rinsing with Milli-Q water and drying under flowing N_2 gas. The dye was desorbed with 1 mL of 1 M NaOH, and its concentration determined from the optical density at 463 nm (Varian, Cary 50). The specific adsorption area of MO on NiO was determined to be 0.18 nm^2 per molecule (Supporting Information). The roughness factor (RF) of the NiO film was calculated by RF = C_{MO} (mol L^{-1}) × 1 mL × N_A × 0.18 nm^2 × $10^{-17}/S$ (cm^2),[27] where C_{MO} is the concentration of the desorbed MO solution, N_A is the Avogadro constant, and S is the geometric face area of NiO film.

Photoelectrochemical measurements were carried out in a standard three-electrode system, consisting of NiO working electrode, Ag/AgCl reference electrode and Pt counter electrode.[28] The electrolyte was 0.1 M $NaClO_4$ aqueous solution saturated with N_2 gas. Irradiation was provided through a 300 W arc xenon lamp (Newport). Linear sweep voltammetry was recorded using potentiostat (Solartron Modulab) scanning at 10 mV s^{-1}. The wavelength-dependent photocurrent response was measured using focused irradiation provided by a 300 W arc xenon lamp (Newport) attached to Oriel 130 1/8 m Cornerstone Monochromator (Newport). Incident photon-to-current conversion efficiency (IPCE) was calculated by IPCE = 1240 × I_{pc} (mA cm^{-2}) × 100 (%)/[λ (nm) × P_i (mW cm^{-2})], where I_{pc} is the photocurrent density and P_i is the power density of the incident light at wavelength λ. Potentiostatic electrochemical impedance spectra (EIS) were measured between 100 kHz and 1 Hz frequency with 5 mV amplitude perturbation. The resultant Nyquist plots were analyzed using commercial ZView software. Photoelectrochemical water splitting was carried out in a sealed dual-chamber Pyrex cell separated by porous glass frit.[29] The NiO working electrode and Ag/AgCl reference electrode were placed in the cathode chamber, and the Pt mesh counter electrode was placed in the anode chamber. The electrolyte (0.1 M $NaClO_4$) in both chambers was prepurged with Ar gas for 30

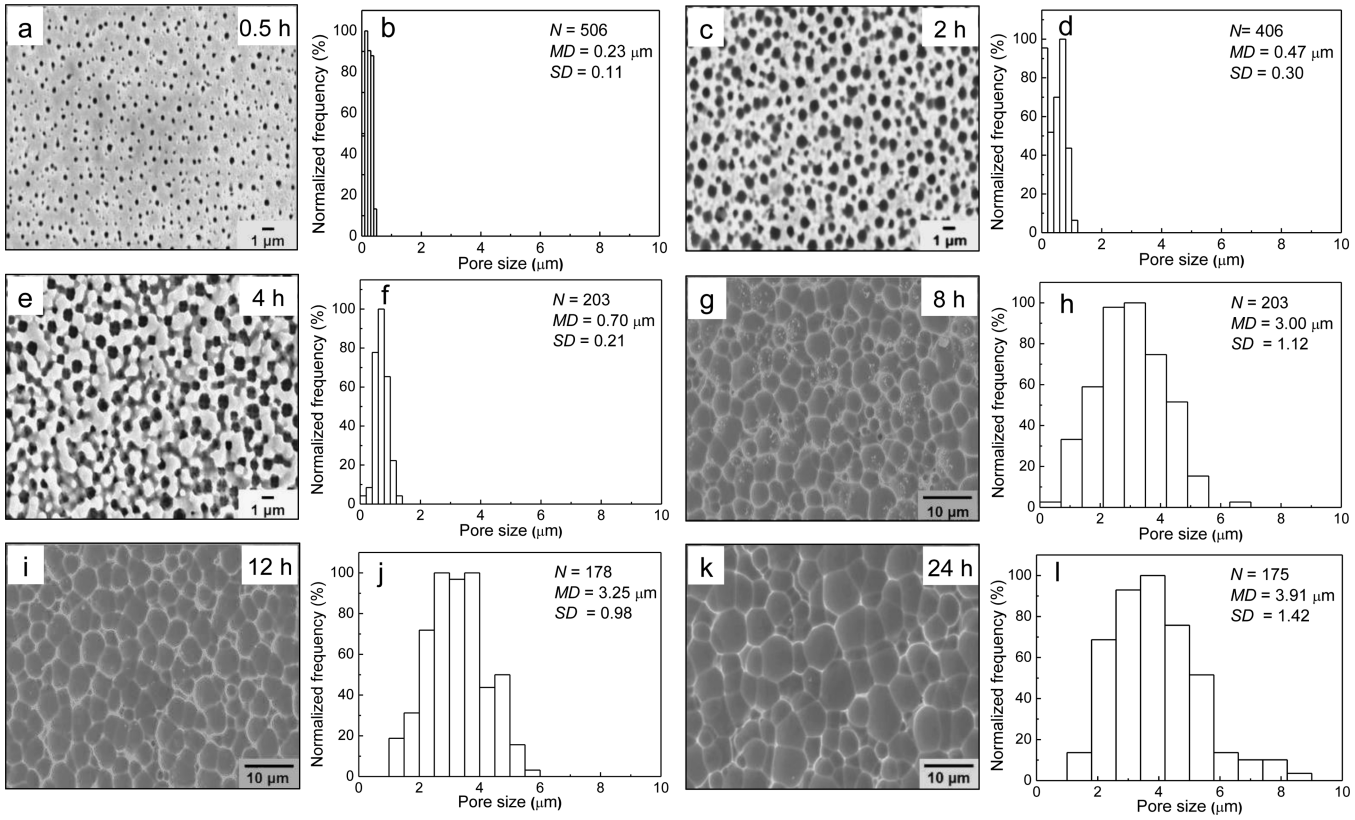

Figure 2. Plan-view images of Ni foils anodized at 60 V for (a) 0.5, (c) 2, (e) 4, (g) 8, (i) 12, and (k) 24 h and (b, d, f, h, j, and l) their respective pore size distributions showing mean diameter (MD) and standard deviation (SD) calculated from sample size (N).

min. The amount of evolved H_2 and O_2 was determined by gas chromatography (Shimadzu GC-8A, molecular sieve 5A column, TCD detector). Photoelectrochemical voltages (E vs Ag/AgCl reference electrode) were converted to the reversible hydrogen electrode (RHE) scale at pH 0 by Nernst equation $E_{RHE} = E_{Ag/AgCl} + 0.059\ pH + E^{\circ}_{Ag/AgCl}$, where $E^{\circ}_{Ag/AgCl}$ is 0.199 V.

3. RESULTS AND DISCUSSION

3.1. Etching-Anodization of Nickel Foil and Physicochemical Characteristics. Metallic nickel foil was anodized in an organic-based alkaline electrolyte containing 0.5 wt % KOH, 5 wt % H_2O, and 94.5 wt % glycerol. Under applied anodization voltages of 40, 50, and 60 V, amorphous nickel hydroxide ($Ni(OH)_2$) and oxyhydroxide (NiOOH) were predominantly formed and etched to create a porous structure. (We will show later by XPS that these phases were indeed formed.) Figure 1a depicts the transient current (J–t) curve during the anodization process at 60 V, which exhibits a three-phase dip-rise-fall pattern that is characteristic of all anodization processes.[30] The initial dip in anodic current was due to the electro-oxidation of metallic nickel (Stage 1, inset of Figure 1a), which was then quickly dominated by the extensive etching-dissolution process (Stage 2, Figure 1a). Typically, etching under an electric field results in one-dimensional (1-D) nanostructures such as that of Fe_2O_3, Ta_2O_5, and TiO_2 nanotubes.[23,25,31] In this case, however, the rapid dissolution of $Ni(OH)_2$ and NiOOH resulted in macroporous structure. Figure 2a–j shows the growth of the structural pore diameter of the anodized Ni from 0.23 μm at 0.5 h to 3.25 μm at 12 h, which encompasses the beginning and near end of Stage 2. The dissolution of $Ni(OH)_2$ under an electric field can be described by the high field model[32] in which Ni–OH bonds are weakened by localized polarization under a high voltage field and Ni^{2+} ions are expelled into the electrolyte. This process results in a porous surface structure.

Stage 3 began after about 16 h of anodization (Figure 1a), at the onset of equilibrium between the rates of electro-oxidation and dissolution.[33] The dissolution rate slowed as the thickness of the walls between pores became limiting (Figure 2k). This is demonstrated in Figure 2l, which shows that the pore size only increased slightly from 3.25 to 3.91 μm in the interval between 12 and 24 h after the start of anodization. For more stable oxides such as TiO_2, Stage 2 is typically much shorter—around 2 min—due to the much more limited dissolution, even in fluoride-based electrolytes.[33] The extensive dissolution of Ni is evidenced by the high cumulative charge density of 460 C cm^{-2} observed during anodization (Figure S1, Supporting Information), which serves as a proxy for the amount of Ni ions expelled into solution. The equivalent measurement for TiO_2 films was just ~1 C cm^{-2} under the same operating voltage. Here, the inherently less stable nature of $Ni(OH)_2$ and NiOOH makes the creation of nanopores or mesopores using direct anodization difficult. There are not many electrolytes that promote a higher rate of oxide/hydroxide formation relative to the rate of dissolution. Our prior attempts to use acidic and fluoridic etchants resulted in too rapid dissolution that no substantial Ni oxide or hydroxide layer could be formed on the substrate.

The rate and extent of Ni dissolution during anodization increases with increasing applied voltage. Figure 1b shows the transient current of NiO films generated during anodization. The increase in magnitude of the transient current as the anodization voltage is increased from 40 to 50 and 60 V tells us

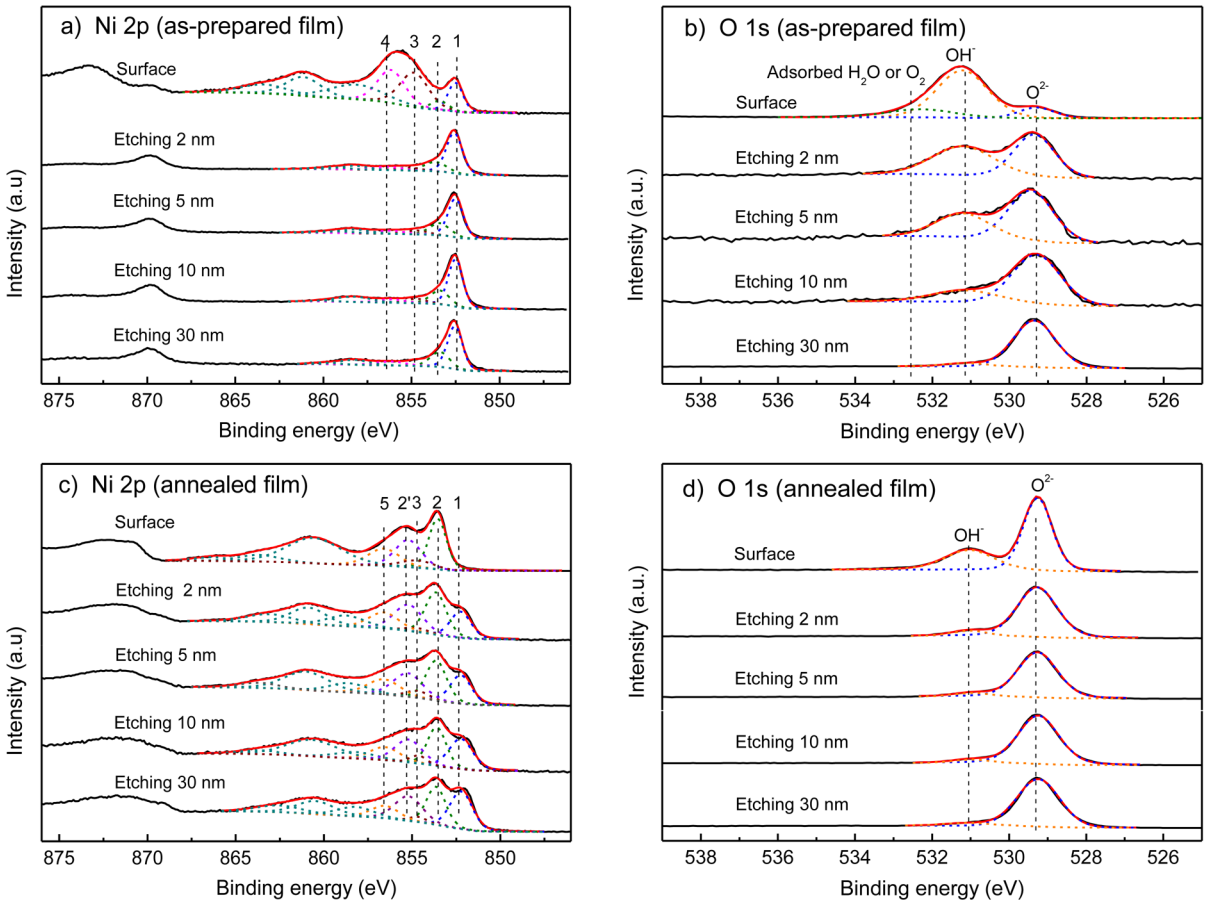

Figure 3. Ni 2p XPS spectra of the (a) as-prepared and (c) annealed NiO electrodes (both samples synthesized by 60 V anodization for 12 h) as a function of etching depth by Ar^+ sputtering. The binding energy peaks are assigned to metallic (1) Ni, (2) NiO, (2′) NiO satellite, (3) $Ni(OH)_2$, (4) NiOOH, and (5) Ni_2O_3. Also shown are the corresponding O 1s XPS spectra for the (b) as-prepared and (d) annealed NiO electrodes. Black solid lines show the measurements, while the red solid lines show the net sum of the deconvoluted peaks of various components (dashed lines).

that the rate of Ni dissolution increases with anodization voltage. Likewise, the area under the transient current curves tells us that the amount of Ni dissolved into the electrolyte also increases with anodization voltage. Mechanistically, the higher applied potential induces greater polarization of the Ni−OH bonds, and hence greater amount of Ni^{2+} ions expelled into the electrolyte. Accordingly, the shifting of peak current to longer anodization time and extended duration of Stage 2 can be understood since the enhanced rate of electro-oxidation under higher applied potential is offset by extensive dissolution until the attainment of steady state. Because more material is expelled into the electrolyte at higher anodization voltages, we see a corresponding increase in the structure pore size during anodization at higher applied voltages. Accordingly, the pore size after 12 h anodization increased from 2.15 to 3.02 to 3.25 μm for applied voltages of 40, 50, and 60 V, respectively (Figure S2, Supporting Information).

Analysis by XPS confirms the predominant formation of $Ni(OH)_2$ and NiOOH on Ni substrates after the alkaline anodization process (Figure 3a). The surface Ni $2p_{3/2}$ spectrum of the as-anodized Ni sample is dominated by the $Ni(OH)_2$ peak at 854.8 eV (39%) and the NiOOH peak at 856.2 eV (37%).[34,35] The generation of NiOOH is attributed to the oxidation of $Ni(OH)_2$ during the anodization process. Some metallic surface Ni (∼17%) is also indicated by the peak at 852.5 eV, alongside shakeup peaks at 858.1, 861.3, and 863.8 eV.[36] This is likely due to excessive localized etching-dissolution. Only a small amount of NiO (6%) was observed in the as-prepared sample. This is expected since the crystallization and conversion to NiO requires thermal annealing of at least 300 °C.[37] The corresponding O 1s spectrum in Figure 3b shows the contributions of lattice oxygen (O^{2-}) at 529.3 eV, adsorbed moisture/molecular oxygen at 532.2 eV, and the expected dominant OH peak at 531.2 eV.[34,38] The significant presence of the OH peak (77% of the measured total oxygen content) corroborates the high surface concentration of $Ni(OH)_2$ and NiOOH. This was further confirmed by the stretching vibration of non-hydrogen bonded OH (ν = 3736 cm^{-1}) measured under FTIR analyses (Figure S3, Supporting Information).

The subsurface features of the anodized sample were studied using *in situ* Ar^+ etching-sputtering. As evident in Figure 3b, the presence of OH groups decreased with increasing depth and was essentially limited to the depth of ∼10 nm. Concomitantly, the XPS peak that corresponds to lattice oxygen from NiO became more prominent. This is consistent with the Ni $2p_{3/2}$ spectrum of the etched surface, which showed a decrease in $Ni(OH)_2$ and NiOOH at the subsurface level.

Annealing the films at 500 °C transforms the $Ni(OH)_2$ and NiOOH groups to NiO. The XPS of the postannealed sample shows a dominant NiO peak at the Ni $2p_{3/2}$ binding energy of 853.5 eV (with satellite peak at 855.2 eV,[35] Figure 3c). The NiO accounts for 53% of the surface composition, while $Ni(OH)_2$ accounts for an additional 15%, the latter of which

dx.doi.org/10.1021/am507138b | ACS Appl. Mater. Interfaces 2014, 6, 18558−18568

can be attributed to the surface OH^- moieties typical of oxide surfaces.[39,40] The conversion of $Ni(OH)_2$ and NiOOH to NiO is also evident in the FTIR measurements: after annealing, the stretching vibration ν = 3736 cm^{-1} disappears and the characteristic stretching vibration of NiO at ν = 550 cm^{-1} appears (Figure S3, Supporting Information).[41] The O 1s XPS measurements were consistent with the Ni $2p_{3/2}$ measurements, revealing the surface composition to be dominated by lattice oxygen with some OH (Figure 3d). Because the OH moieties of the annealed sample are limited to the surface, the corresponding XPS peak essentially disappeared beyond the depth of 10 nm. An interesting observation is the formation of Ni_2O_3 (surface composition 32%, binding energy 856.6 eV),[42] which can be traced to the dehydroxylation/decomposition of NiOOH[34] or the oxidation of surface Ni^{2+} during high-temperature treatment.[42,43] Its composition decreased gradually with increasing depth but remained significant (17%) even at the depth of 30 nm.

The bulk formation of crystallized NiO films from the anodized Ni was further examined by XRD after annealing at 300, 400, 500, and 600 °C (Figure 4). At 300 °C, only metallic

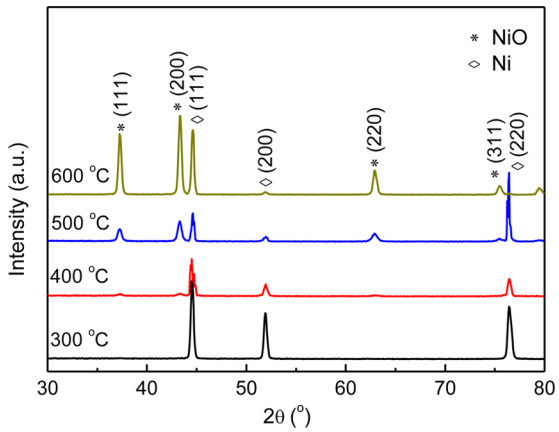

Figure 4. XRD patterns of anodized NiO (60 V, 12 h anodization) after annealing at 300, 400, 500, and 600 °C (ramping 5 °C min^{-1}) for 6 h in air.

Ni substrate was measured, indicating the anodized NiO_x layer was still in an amorphous state. From 400 °C, three diffraction peaks appear at 37.3, 43.3 and 62.9° belonging to the (111), (200), and (220) crystal planes of cubic NiO (JCPDF: 47-1049), respectively. Since the $Ni(OH)_2$ was limited to the surface, it was not detected by XRD. At the same time, the Ni_2O_3 phase was also not detectable by XRD despite being evident under XPS, inferring that it was either highly dispersed or existing as amorphous. The Scherrer-determined NiO crystallite size increased from 15 to 21 to 27 nm with increasing annealing temperature from 400 to 500 to 600 °C, respectively, as a result of solid-state sintering at high temperature.

The surface RF of the anodized NiO films was measured by the Langmuir adsorption of MO, which we had predetermined to have adsorption area of 0.18 nm^2 NiO per MO molecule (Figure S4, Supporting Information). The RF is defined as the ratio of the actual surface area of the NiO material to the area of the two-dimensional plane defined by the boundaries of the electrode (or the geometry face area). As shown in Figure 5a, the nucleation of small pits after 0.5 h of anodization (Figure 2a) resulted in RF of 1.7. After 2 h, the RF increased to 5.2 as a result of extended dissolution along the pore depth and thinning of the walls. After 4 h, the RF decreased to 3.2. This trend of decreased RF with anodization time is unique for NiO and has not been observed for other anodization-prepared films such as TiO_2.[44] In our case, the decrease in RF coincides with the peak transient current seen in Figure 1a, which corresponds to the fastest Ni dissolution rate relative to that of Ni oxidation. This is likely to result in decreased pore depth, as reflected from the surface patches dissolution (Figure 2e), and to a lesser extent the simultaneous thinning of sidewalls (i.e., widening of the pores). When the oxidation layer growth became limited past the dissolution peak, dissolution was compensated by pronounced etching of sidewalls, as revealed by the significant increase in pore diameter at 8 h (Figure 2h). This is followed by the increase in exposed surface area up to RF 8.4 at 12 h. After 24 h anodization, significant loss of sidewalls due to overdissolution resulted in the RF decreasing to 3.9 after. Increasing the anodization voltage from 40 to 60 V essentially doubled the RF at 12 h of anodization (Figure 5b), consistent with the trend of increasing pore size due to sidewalls thinning.

3.2. Photoelectrochemical (PEC) Properties of Anodized NiO Electrodes. The anodized NiO samples were characterized in a standard three-electrode system with

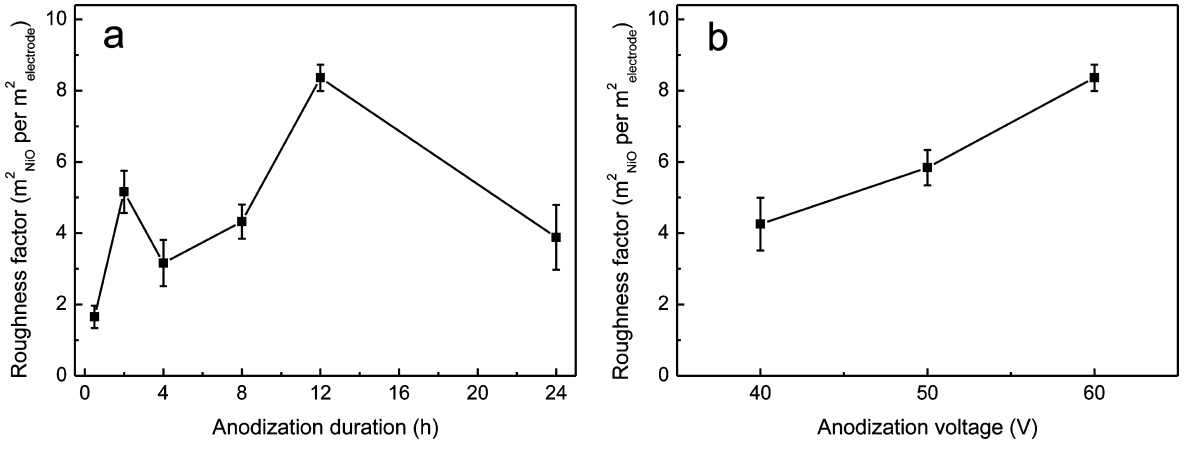

Figure 5. Roughness factor of NiO prepared (a) at anodization voltage of 60 V for different durations and (b) at different voltages for 12 h. All samples were annealed at 500 °C for 6 h in air.

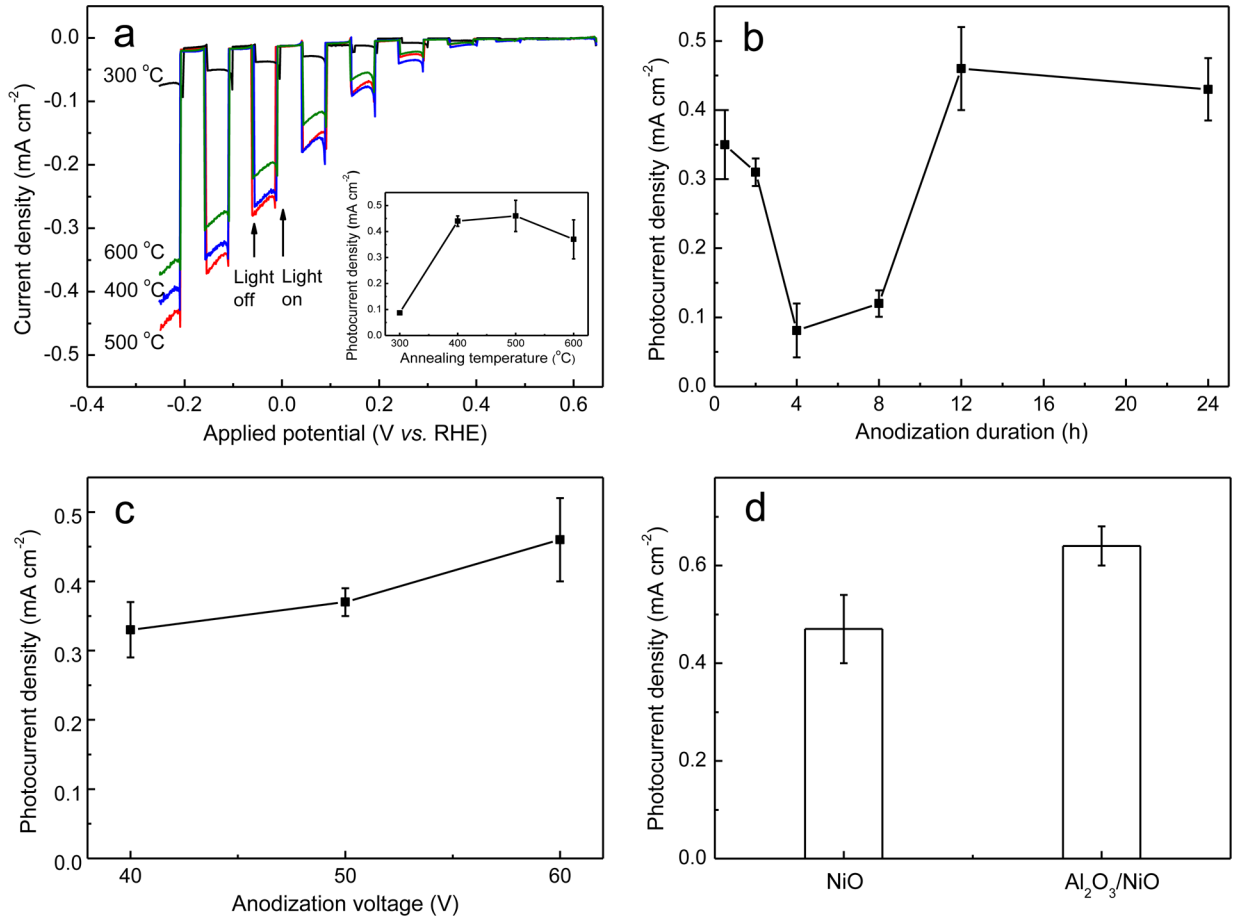

Figure 6. (a) Linear sweep voltammetry of NiO electrodes (60 V, 12 h anodization) under chopping mode; (inset) photocurrent density of the electrodes at different annealing temperatures. (b) Photocurrent density of NiO electrodes prepared at 60 V (annealed 500 °C) as a function of anodization duration and (c) for 12 h duration (annealed 500 °C) but at different anodization voltages. (d) Photocurrent density of NiO electrodes (60 V, 12 h anodization, annealed 500 °C) with and without Al_2O_3 layer coating. All photocurrent densities in the inset of a and in panels b, c, and d are compared at −0.25 V vs RHE.

Table 1. Fitting Parameters Derived from the Electrochemical Impedance Spectroscopy of NiO Electrodes Prepared and Measured under Different Conditions, and Their Photoelectrocatalytic Turnover Frequencies for Water Reduction

				EIS[a]			
sample	anodization duration (h)	anodization voltage (V)	electrochemical potential (V vs RHE)[b]	R_s (kΩ)	R_{ct} (kΩ)	CPE (μF)	TOF (× 10^{-3} s^{-1})[c]
NiO[d]	0.5	60	−0.25	0.22	10.1	0.5	577
	2	60	−0.25	0.28	10.5	0.5	169
	4	60	−0.25	0.27	15.3	0.7	70
	8	60	−0.25	0.25	14.4	0.9	76
	12	60	−0.25	0.20	4.6	1.5	150
	24	60	−0.25	0.31	8.1	0.3	301
	12	40	−0.25	0.20	7.5	1.1	211
	12	50	−0.25	0.20	7.4	1.0	173
	12	60	0	0.28	6.6	2.3	72
	12	60	+0.15	0.26	7.3	3.9	31
	12	60	+0.35	0.25	19.3	8.0	6
	12	60	+0.55	0.34	104.8	20.3	1
Al_2O_3/NiO	12	60	−0.25	0.31	3.4	2.0	208

[a]Electrochemical impedance spectroscopy, see Figure 7a (inset) for equivalent circuit. [b]Measured in three-electrode system. [c]Turnover frequencies, TOF, calculated from the net photocurrent ($2H^+ + 2e^- \rightarrow H_2$) and the number of NiO surface sites (Supporting Information). [d]Anodized NiO samples were annealed at 500 °C.

deaerated 0.1 M $NaClO_4$ aqueous electrolyte. Figure 6a depicts the cathodic photocurrent response of the NiO electrodes, which is typical of *p*-type semiconductors.[13,15,45] The onset potential of the anodized NiO was measured at +0.53 V versus RHE (Figure S5, Supporting Information), consistent with the expected Fermi level of *p*-NiO,[46] and the valence band edge is

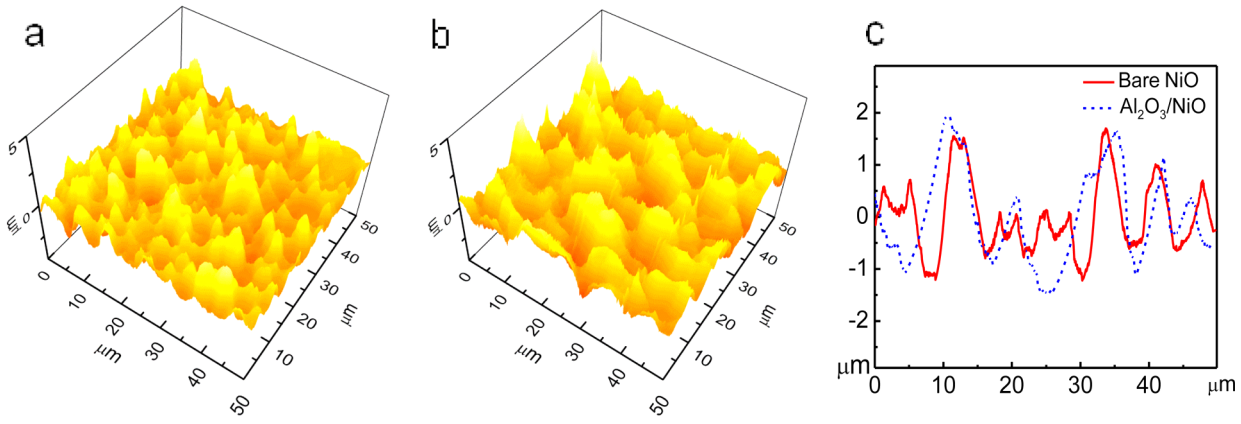

Figure 7. AFM images showing the three-dimensional topology of (a) NiO electrode (60 V, 12 h anodization, annealed at 500 °C) and (b) that with Al_2O_3 layer coating. (c) Representative depth profiles of the two electrodes.

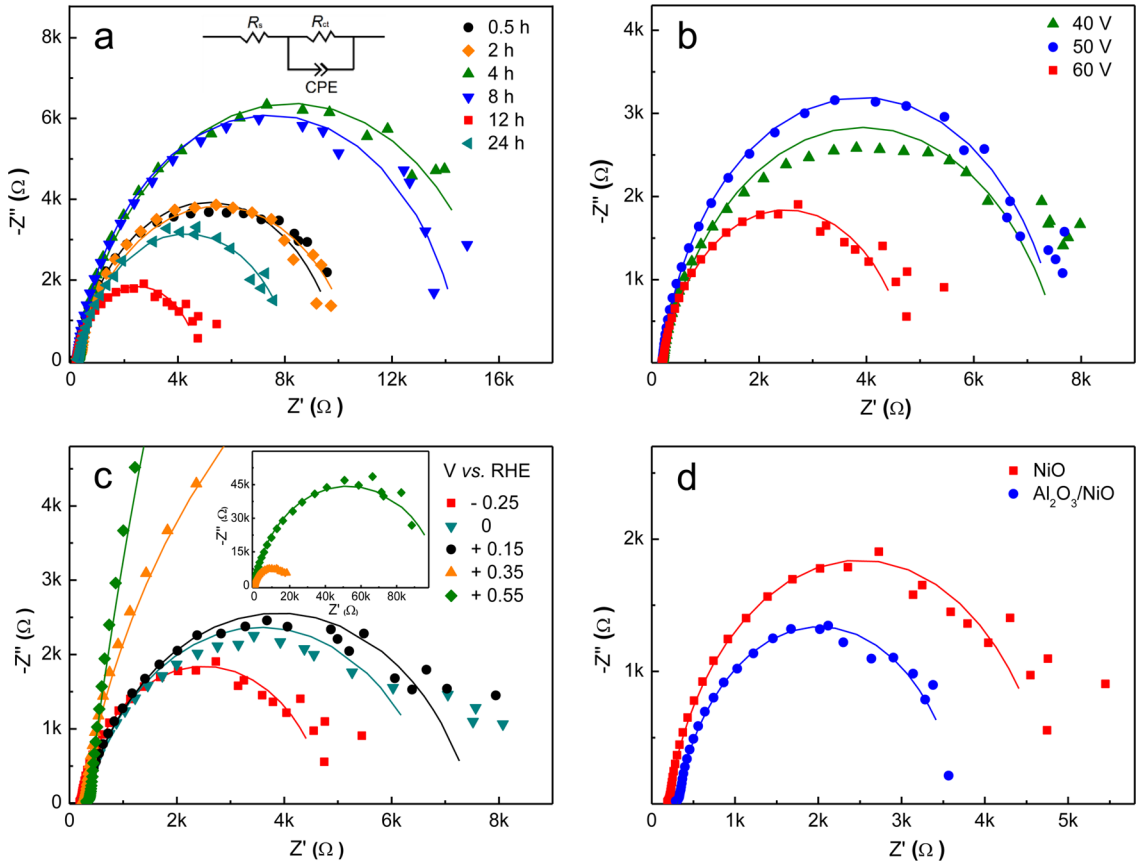

Figure 8. Nyquist plots measured at −0.25 V vs RHE of NiO electrodes prepared (a) at 60 V for different anodization durations and (inset) equivalent circuit used for spectra fittings; and (b) that at different anodization voltages for 12 h. (c) Nyquist plots of NiO electrode (60 V, 12 h anodization) measured at different bias potentials and (inset) full spectra at +0.55 V and +0.35 V vs RHE. (d) Nyquist plots measured at −0.25 V vs RHE of NiO electrodes with and without Al_2O_3 layer coating.

approximately +0.4 V below this level.[47] As evident in Figure 6a, the sample annealed at 300 °C produced a low photocurrent density of 0.09 mA cm^{-2} (at −0.25 V vs RHE) due to its amorphous structure. Increasing the annealing temperature to 500 °C increased the photocurrent density to 0.46 mA cm^{-2} as a result of improved crystallization. In general, high crystalinity is required for efficient photocurrent generation; the less crystalline a material, the more defect sites exist to induce recombination of charge carriers.[48,49] At 600 °C, the sintering of NiO resulted in the loss of surface area as well as the regular pore structure (Figure S6, Supporting Information), yielding lower photocurrent density due to the decreased area of the semiconductor-electrolyte interface.[50,51] The effect of anodization duration on the photocurrent density of NiO is depicted in Figure 6b. The low photocurrent density measured after 4 h of anodization is consistent with the low RF shown earlier. The photocurrent density increases gradually with anodization time before reaching a maximum value at 12 h anodization.

dx.doi.org/10.1021/am507138b | ACS Appl. Mater. Interfaces 2014, 6, 18558−18568

Scheme 1. Energy Diagram of Photoexcited *p*-NiO (a) without and (b) with Cathodic Bias

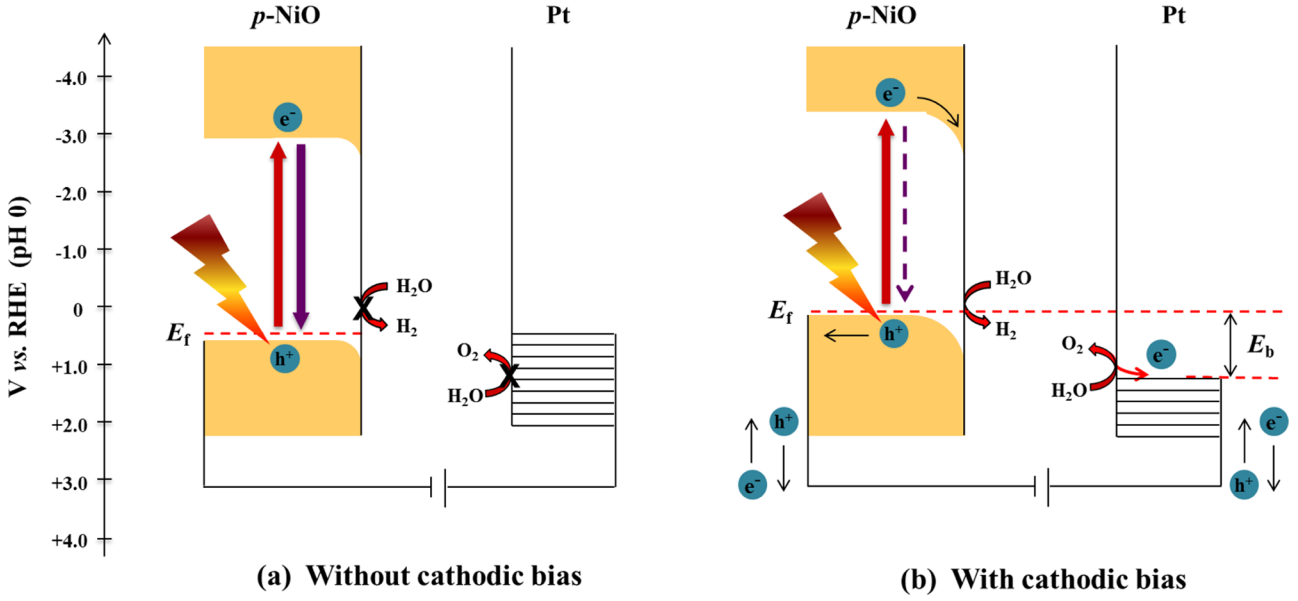

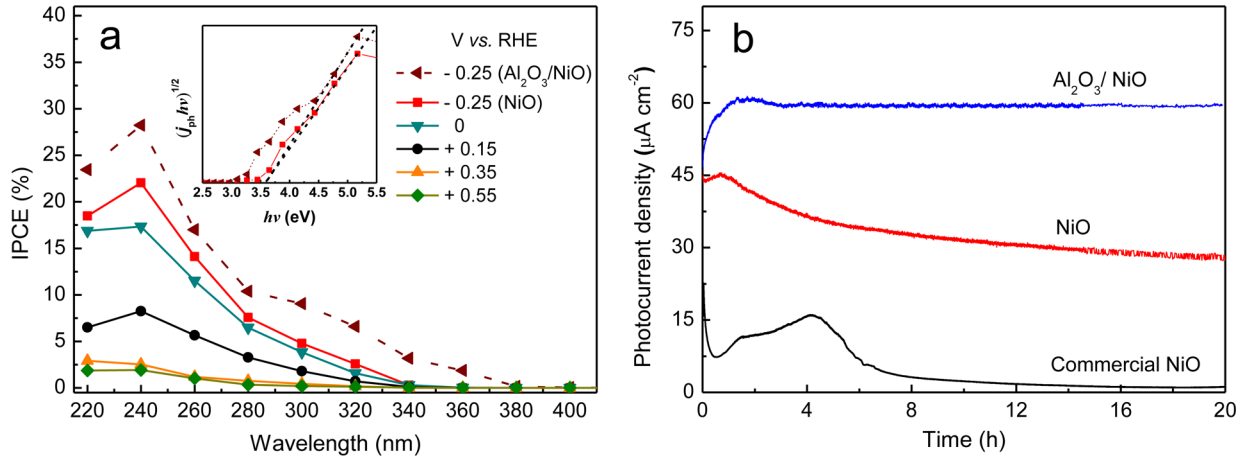

Figure 9. (a) IPCE profiles of the anodized NiO photoelectrode at different applied potentials (solid lines) and Al_2O_3/NiO electrode (broken line) at −0.25 V vs RHE. (Inset) Tauc plot of NiO and Al_2O_3/NiO electrodes; the extension of the linear portion of the curves converges at the NiO intrinsic bandgap of 3.6 eV. (b) The durability of different NiO electrodes under full arc xenon lamp (300 W) and −0.25 V vs RHE. All of the anodized NiO electrodes were prepared at 60 V for 12 h, followed by annealing at 500 °C for 6 h. The optimum loading of the commercial NiO on FTO is 6 mg cm^{-2} (Supporting Information).

Essentially, the photocurrent density is dependent on the amount of semiconductor-electrolyte interface and the quality of the NiO surface sites for which the charge transfer, or more specifically the transfer of photoelectrons to protons for water reduction, takes place efficiently. The amount of semiconductor−electrolyte interface can be reflected by the RF values, and the quality of the charge transfer sites by the turnover frequencies (TOF; Table 1) of the NiO electrodes. The optimization of both parameters is essential to achieve high photocurrent. For example, NiO electrodes anodized for 0.5 h had the highest measured TOF (577×10^{-3} s^{-1}) but the lowest RF (1.7) and generated a photocurrent of 0.35 mA cm^{-2}. Electrodes anodized for 12 h had a lower TOF of 150×10^{-3} s^{-1} but a much higher RF of 8.4 and generated 0.46 mA cm^{-2}. As the rate of transfer of minority carriers across NiO surface improves, a higher rate of net photoholes separation (or cathodic photocurrent) can be measured in the external circuit. Figure 6c shows the increasing photocurrent density (0.33 to 0.37 to 0.46 mA cm^{-2}) with increasing anodization voltage (40 to 50 to 60 V) arising from the increased RF (4.3, 5.8, and 8.4, respectively). Clearly, the photocurrent response is not proportional to RF considering the decreasing TOF of 211×10^{-3}, 173×10^{-3}, and 150×10^{-3} s^{-1} in the same order, which is related to the coinfluence of sidewall thickness and the associated charge transfer efficiency.

Coating NiO films anodized for 12 h at 60 V with a thin layer of Al_2O_3 (via hydrolysis of aluminum trisec-butoxide) increases the photocurrent density from 0.46 to 0.64 mA cm^{-2} (Figure 6d). This increase is due to a measured increase in the TOF from 150×10^{-3} to 208×10^{-3} s^{-1}. The Al_2O_3 blocking layer is commonly employed in dye-sensitized solar cells as a tunneling barrier that reduces the back-recombination of photoelectrons at the semiconductor interface.[52] In the current study, the Al_2O_3 layer allows the tunneling of photoelectrons to its surface for water reduction to take place, thereby passivating the surface charge recombination on the NiO surface. As we will

dx.doi.org/10.1021/am507138b | ACS Appl. Mater. Interfaces 2014, 6, 18558−18568

show later, the Al_2O_3 coating also serves to stabilize the NiO photoelectrode under prolonged photoexcitation. Characterization by atomic force microscopy (AFM, Figure 7) and further by FE-SEM (Figure S7, Supporting Information) confirms the original morphology of NiO is retained after coating with Al_2O_3 blocking layer.

Figure 8 shows the Nyquist plots from the electrochemical impedance spectroscopy (EIS) of the NiO electrodes. In every case, a single depressed semicircle can be measured under photoexcitation and adequately fitted with an equivalent circuit, comprising of electrolyte resistance (R_s) connected in series to an RC circuit describing the charge transfer resistance at the semiconductor-electrolyte interface (R_{ct}) and constant phase element (CPE) (Figure 8a, inset).[53] Table 1 summarizes the fitting parameters of R_s, R_{ct}, and CPE. Here, one can see that the decrease in R_{ct} of the NiO electrodes in Figure 8a,b is in accordance with the increase in photocurrent density shown in Figure 6b,c. This reiterates the importance of a large semiconductor-electrolyte interface area and the quality of surface sites on the net charge separation efficiencies. By increasing the potential bias negatively from +0.55 to −0.25 V versus RHE, the resultant energy levels were made favorable, and the semiconductor-electrolyte interfacial resistance decreases, thereby increasing the cathodic photocurrent density (Figure 8c). With NiO valence band edge potential of +0.93 V versus RHE (pH 0), it is inadequate to oxidize water (+1.23 V vs RHE) in its unbiased state. Cathodic bias of at least 0.3 V more negative than the quasi-Fermi level (i.e., E_f (+0.53 V vs RHE) − E_b (0.30 V) = +0.23 V vs RHE) is necessary to induce sufficient band bending so that holes oxidation of water can take place at the Pt counter electrode (Scheme 1). This is evident in Figure 8c and Table 1 where the applied potential that is more negative than +0.15 V versus RHE saw a significant decrease in R_{ct} values. Figure 8d shows further decrease in the R_{ct} of NiO upon coating of Al_2O_3 barrier layer that allows the tunneling of photoelectrons to the electrode surface for water reduction while suppressing the back recombination with photoholes on the NiO surface.[54]

3.3. Photoelectrochemical Water Splitting. The incident photon-to-current conversion efficiency (IPCE) of the optimized NiO electrode (60 V, 12 h) as a function of applied potential is shown in Figure 9a. By extension of the linear portion of the $(j_{ph}h\nu)^{1/n}$ versus $h\nu$ curve to abscissa[55] (j_{ph} is the photocurrent generated per incident photon, n = 2 for an indirect bandgap semiconductor),[41] the bandgap of NiO was estimated to be 3.6 eV (Figure 9a, inset). This is in agreement with the theoretical bandgap of NiO (3.6−4.0 eV).[56] Relatively low IPCE values of less than 3% were measured under applied potentials of +0.55 and +0.35 V versus RHE which, as mentioned earlier, is insufficient for water oxidation at the counter electrode. The trace IPCE values may have originated from the oxidation of water by deep holes in the valence band. With sufficient band bending, significant enhancement in IPCE could be seen under more negative potential bias from +0.15 to −0.25 V versus RHE, yielding maximum IPCE values of 8.3 to 22%, respectively, at 240 nm. Coating the NiO with an Al_2O_3 blocking layer enhances the overall IPCE of electrode, with a maximum IPCE of 28% at −0.25 V versus RHE.

We assessed the stability of the anodized NiO electrodes by comparing their generated photocurrent under continuous irradiation against that of a reference electrode fabricated from commercial NiO nanoparticles (see Figure S8, Supporting Information, for detailed optimization). The measured photocurrent over the course of irradiation reflects the rate of holes generated and separated at the photocathode chamber and transported to the Pt counter electrode through the external circuit. As shown in Figure 9b, the photocurrent generated by the anodized NiO electrode starts at 45 μA cm^{-2} and then gradually decreases for 16 h before stabilizing at 26 μA cm^{-2} — a degradation of 42%. The decrease in photocurrent can be traced to the conversion of NiO into NiOOH by oxidation-hydroxylation (increased to 55%) at the expense of NiO (decreased from 53 to 15%; Figure S9, Supporting Information).

Adding an Al_2O_3 blocking layer significantly improves the stability of the NiO film. The Al_2O_3/NiO electrode generated 60 μA cm^{-2} consistently throughout the 20 h irradiation. No significant changes to the NiO states were measured before and after the irradiation period (Figure S9, Supporting Information). Hence, the role Al_2O_3 layer is 2-fold: (1) it acts as a tunneling barrier that suppresses the back-recombination of photoelectrons at the NiO surface, and (2) it chemically insulates the NiO layer from oxidation and aqueous dissolution during photoirradiation.

Analysis of the amount of gaseous H_2 and O_2 produced by both NiO and Al_2O_3/NiO electrodes shows that both have Faraday efficiencies of 100 ± 2% (Table 2), consistent with our earlier work using the same cell.[29] The ratio of generated H_2 to O_2 was 2.1−2.2:1, which is close to the theoretical 2:1 ratio expected for water splitting reactions. On the other hand, electrodes fabricated with commercial NiO nanoparticles exhibited a drastic drop in photocurrent, which was accompanied by a photodissolution hump between 0.5 to 7.5 h. The accumulation of majority charge carriers in the electrode due to poor transport may have resulted in this photodissolution. The H_2-to-O_2 ratio was found to be 2.6:1, where higher H_2 evolution would be expected due to the dissolution of NiO.

Table 2. Evolved Gaseous H_2 and O_2 and Faradaic Efficiency of Photoelectrochemical Water Splitting over Different NiO Electrodes

photoelectrode	gaseous evolution (20 h irradiation)			Faradaic efficiency (%)[c]
	H_2[a]	O_2[b]	H_2:O_2	
	(μmol cm$^{-2}_{electrode}$)			
Al_2O_3/NiO	21.8	10.4	2.1	102.0
anodized NiO	12.3	5.5	2.2	100.5
commercial NiO[d]	1.9	0.8	2.6	98.5

[a]Evolved H_2 in cathode chamber measured by gas chromatography. [b]Evolved O_2 in anode chamber measured by gas chromatography. [c]Faradaic efficiency calculated based on H_2 evolution. [d]Commercial (Aldrich) Nano NiO powder on FTO. Refer to Supporting Information for the electrode optimization.

4. CONCLUSIONS

We have developed a way to synthesize porous *p*-NiO photoelectrodes that is based on the anodization of nickel foil in an alkaline electrolyte. The alkaline-based synthesis presents an alternative methodology to the conventional anodization synthesis of materials that are otherwise incompatible with conventional acidic and fluoride-based electrolytes. We found that the optimization of the roughness factor and the quality of

NiO surface sites are critical to the interfacial charge (minority carrier) transfer of the photocathode and vital toward obtaining high photocurrent efficiencies. Adding a thin Al_2O_3 blocking layer on top of the NiO layer further improves the photoelectrochemical water splitting efficiency of the electrode by functioning as a tunnelling barrier. The Al_2O_3 blocking layer also enhances the photoelectrode chemical stability under prolonged photoexcitation. Such high-efficiency anodized NiO electrodes should be suitable for other *p*-type photoelectrochemical applications including photovoltaic solar cells, organic light-emitting diodes, field-effect transistors, and tandem *p*/*n*-type devices in general.

■ ASSOCIATED CONTENT

Supporting Information

Arithmetic and geometric pore size distribution of NiO electrodes anodized under different conditions; SEM images of NiO electrodes anodized at different voltages and annealed at different temperatures; FTIR analyses of NiO electrodes; adsorption isotherm of methyl orange on commercial NiO nanoparticles; linear sweep voltammetry of NiO electrode; optimization fabrication of commercial NiO electrode; XPS of NiO and Al_2O_3 electrodes after photoelectrochemical water splitting; determination of turnover frequencies (TOFs). This material is available free of charge via the Internet at http://pubs.acs.org.

■ AUTHOR INFORMATION

Corresponding Author

*E-mail: wyteoh@cityu.edu.hk.

Notes

The authors declare no competing financial interest.

■ ACKNOWLEDGMENTS

The authors thank Tak Fu Hung and Kam Wa Wong of the Department of Physics and Materials Science, City University of Hong Kong, for their assistance with XPS and SEM measurements, respectively. This work was supported through the financial assistance of Hong Kong Research Grant Council through the General Research Funds (CityU 103311 and 104812) and City University of Hong Kong through the Strategic Research Grant (7004003).

■ REFERENCES

(1) O'Regan, B.; Grätzel, M. A Low-Cost, High-efficiency Solar Cell Based on Dye-Sensitized Colloidal TiO_2 Films. *Nature* **1991**, *353*, 737−740.

(2) Fujishima, A.; Honda, K. Electrochemical Photolysis of Water at a Semiconductor Electrode. *Nature* **1972**, *238*, 37−38.

(3) Ng, C.; Iwase, A.; Ng, Y. H.; Amal, R. Understanding Self-Photorechargeability of WO_3 for H_2 Generation without Light Illumination. *ChemSusChem* **2013**, *6*, 291−298.

(4) Seabold, J. A.; Choi, K.-S. Effect of a Cobalt-based Oxygen Evolution Catalyst on the Stability and the Selectivity of Photo-Oxidation Reactions of a WO_3 Photoanode. *Chem. Mater.* **2011**, *23*, 1105−1112.

(5) Bang, J. H.; Kamat, P. V. Solar Cells by Design: Photoelectrochemistry of TiO_2 Nanorod Arrays Decorated with CdSe. *Adv. Funct. Mater.* **2010**, *20*, 1970−1976.

(6) Yang, X.; Wolcott, A.; Wang, G.; Sobo, A.; Fitzmorris, R. C.; Qian, F.; Zhang, J. Z.; Li, Y. Nitrogen-Doped ZnO Nanowire Arrays for Photoelectrochemical Water Splitting. *Nano Lett.* **2009**, *9*, 2331−2336.

(7) Sivula, K.; Le Formal, F.; Grätzel, M. Solar Water Splitting: Progress Using Hematite (α-Fe_2O_3) Photoelectrodes. *ChemSusChem* **2011**, *4*, 432−449.

(8) Jia, Q. X.; Iwashina, K.; Kudo, A. Facile Fabrication of an Efficient $BiVO_4$ Thin Film Electrode for Water Splitting Under Visible Light Irradiation. *Proc. Natl. Acad. Sci. U.S.A.* **2012**, *109*, 11564−11569.

(9) Heller, A. Conversion of Sunlight into Electrical Power and Photoassisted Electrolysis of Water in Photoelectrochemical Cells. *Acc. Chem. Res.* **1981**, *14*, 154−162.

(10) Bard, A. J.; Faulkner, L. R. *Electrochemical Methods: Fundamentals and Applications*, 2nd ed.; Wiley: New York, 2001.

(11) Zhang, Z. Y.; Shao, C. L.; Li, X. H.; Wang, C. H.; Zhang, M. Y.; Liu, Y. C. Electrospun Nanofibers of *p*-Type NiO/*n*-Type ZnO Heterojunctions with Enhanced Photocatalytic Activity. *ACS Appl. Mater. Interfaces* **2010**, *2*, 2915−2923.

(12) Paracchino, A.; Laporte, V.; Sivula, K.; Grätzel, M.; Thimsen, E. Highly Active Oxide Photocathode for Photoelectrochemical Water Reduction. *Nat. Mater.* **2011**, *10*, 456−461.

(13) Read, C. G.; Park, Y.; Choi, K. S. Electrochemical Synthesis of *p*-Type $CuFeO_2$ Electrodes for Use in a Photoelectrochemical Cell. *J. Phys. Chem. Lett.* **2012**, *3*, 1872−1876.

(14) Iwashina, K.; Kudo, A. Rh-Doped $SrTiO_3$ Photocatalyst Electrode Showing Cathodic Photocurrent for Water Splitting under Visible-Light Irradiation. *J. Am. Chem. Soc.* **2011**, *133*, 13272−13275.

(15) Cao, J.; Zhang, Y.; Liu, L.; Ye, J. A *p*-Type Cr-Doped TiO_2 Photo-Electrode for Photo-Reduction. *Chem. Commun.* **2013**, *49*, 3440−3442.

(16) Liu, J.; Hisatomi, T.; Ma, G.; Iwanaga, A.; Minegishi, T.; Moriya, Y.; Katayama, M.; Kubota, J.; Domen, K. Improving the Photoelectrochemical Activity of $La_5Ti_2CuS_5O_7$ for Hydrogen Evolution by Particle Transfer and Doping. *Energy Environ. Sci.* **2014**, *7*, 2239−2242.

(17) Nattestad, A.; Mozer, A. J.; Fischer, M. K. R.; Cheng, Y. B.; Mishra, A.; Bauerle, P.; Bach, U. Highly Efficient Photocathodes for Dye-Sensitized Tandem Solar Cells. *Nat. Mater.* **2010**, *9*, 31−35.

(18) Tong, L.; Iwase, A.; Nattestad, A.; Bach, U.; Weidelener, M.; Gotz, G.; Mishra, A.; Bauerle, P.; Amal, R.; Wallace, G. G.; Mozer, A. J. Sustained Solar Hydrogen Generation Using a Dye-Sensitised NiO Photocathode/$BiVO_4$ Tandem Photo-Electrochemical Device. *Energy Environ. Sci.* **2012**, *5*, 9472−9475.

(19) Wu, X. Y.; Xing, G. C.; Tan, S. L. J.; Webster, R. D.; Sum, T. C.; Yeow, E. K. L. Hole Transfer Dynamics from Dye Molecules to *p*-Type NiO Nanoparticles: Effects of Processing Conditions. *Phys. Chem. Chem. Phys.* **2012**, *14*, 9511−9519.

(20) Powar, S.; Wu, Q.; Weidelener, M.; Nattestad, A.; Hu, Z.; Mishra, A.; Bauerle, P.; Spiccia, L.; Cheng, Y.-B.; Bach, U. Improved Photocurrents for *p*-Type Dye-Sensitized Solar Cells Using Nano-Structured Nickel(II) Oxide Microballs. *Energy Environ. Sci.* **2012**, *5*, 8896−8900.

(21) Gibson, E. A.; Le Pleux, L.; Fortage, J.; Pellegrin, Y.; Blart, E.; Odobel, F.; Hagfeldt, A.; Boschloo, G. Role of the Triiodide/Iodide Redox Couple in Dye Regeneration in *p*-Type Dye-Sensitized Solar Cells. *Langmuir* **2012**, *28*, 6485−6493.

(22) Roy, P.; Berger, S.; Schmuki, P. TiO_2 Nanotubes: Synthesis and Applications. *Angew. Chem., Int. Ed.* **2011**, *50*, 2904−2939.

(23) Mohapatra, S. K.; John, S. E.; Banerjee, S.; Misra, M. Water Photooxidation by Smooth and Ultrathin α-Fe_2O_3 Nanotube Arrays. *Chem. Mater.* **2009**, *21*, 3048−3055.

(24) Wei, W.; Lee, K.; Shaw, S.; Schmuki, P. Anodic Formation of High Aspect Ratio, Self-Ordered Nb_2O_5 Nanotubes. *Chem. Commun.* **2012**, *48*, 4244−4246.

(25) El-Sayed, H. A.; Birss, V. I. Controlled Interconversion of Nanoarray of Ta Dimples and High Aspect Ratio Ta Oxide Nanotubes. *Nano Lett.* **2009**, *9*, 1350−1355.

(26) Palomares, E.; Clifford, J. N.; Haque, S. A.; Lutz, T.; Durrant, J. R. Control of Charge Recombination Dynamics in Dye Sensitized Solar Cells by the Use of Conformally Deposited Metal Oxide Blocking Layers. *J. Am. Chem. Soc.* **2003**, *125*, 475−482.

(27) Kay, A.; Cesar, I.; Gratzel, M. New Benchmark for Water Photooxidation by Nanostructured α-Fe_2O_3 Films. *J. Am. Chem. Soc.* **2006**, *128*, 15714−15721.
(28) Yang, H.; Kershaw, S. V.; Wang, Y.; Gong, X.; Kalytchuk, S.; Rogach, A. L.; Teoh, W. Y. Shuttling Photoelectrochemical Electron Transport in Tricomponent CdS/rGO/TiO_2 Nanocomposites. *J. Phys. Chem. C* **2013**, *117*, 20406−20414.
(29) Kho, Y. K.; Iwase, A.; Teoh, W. Y.; Madler, L.; Kudo, A.; Amal, R. Photocatalytic H_2 Evolution over TiO_2 Nanoparticles. The Synergistic Effect of Anatase and Rutile. *J. Phys. Chem. C* **2010**, *114*, 2821−2829.
(30) Allam, N. K.; Feng, X. J.; Grimes, C. A. Self-Assembled Fabrication of Vertically Oriented Ta_2O_5 Nanotube Arrays, and Membranes Thereof, by One-Step Tantalum Anodization. *Chem. Mater.* **2008**, *20*, 6477−6481.
(31) Yoriya, S.; Paulose, M.; Varghese, O. K.; Mor, G. K.; Grimes, C. A. Fabrication of Vertically Oriented TiO_2 Nanotube Arrays Using Dimethyl Sulfoxide Electrolytes. *J. Phys. Chem. C* **2007**, *111*, 13770−13776.
(32) Allam, N. K.; Grimes, C. A. Electrochemical Fabrication of Complex Copper Oxide Nanoarchitectures via Copper Anodization in Aqueous and Non-Aqueous Electrolytes. *Mater. Lett.* **2011**, *65*, 1949−1955.
(33) Yun, J. H.; Ng, Y. H.; Ye, C. H.; Mozer, A. J.; Wallace, G. G.; Amal, R. Sodium Fluoride-Assisted Modulation of Anodized TiO_2 Nanotube for Dye-Sensitized Solar Cells Application. *ACS Appl. Mater. Interfaces* **2011**, *3*, 1585−1593.
(34) Ratcliff, E. L.; Meyer, J.; Steirer, K. X.; Garcia, A.; Berry, J. J.; Ginley, D. S.; Olson, D. C.; Kahn, A.; Armstrong, N. R. Evidence for Near-Surface NiOOH Species in Solution-Processed NiO_x Selective Interlayer Materials: Impact on Energetics and the Performance of Polymer Bulk Heterojunction Photovoltaics. *Chem. Mater.* **2011**, *23*, 4988−5000.
(35) Peck, M. A.; Langell, M. A. Comparison of Nanoscaled and Bulk NiO Structural and Environmental Characteristics by XRD, XAFS, and XPS. *Chem. Mater.* **2012**, *24*, 4483−4490.
(36) Biesinger, M. C.; Payne, B. P.; Lau, L. W. M.; Gerson, A.; Smart, R. S. C. X-ray Photoelectron Spectroscopic Chemical State Quantification of Mixed Nickel Metal, Oxide, and Hydroxide Systems. *Surf. Interface Anal.* **2009**, *41*, 324−332.
(37) Kim, S.-I.; Lee, J.-S.; Ahn, H.-J.; Song, H.-K.; Jang, J.-H. Facile Route to an Efficient NiO Supercapacitor with a Three-Dimensional Nanonetwork Morphology. *ACS Appl. Mater. Interfaces* **2013**, *5*, 1596−1603.
(38) Zhang, X.; Ptasinska, S. Dissociative Adsorption of Water on an H_2O/GaAs(100) Interface: In Situ Near-Ambient Pressure XPS Studies. *J. Phys. Chem. C* **2014**, *118*, 4259−4266.
(39) Cappus, D.; Xu, C.; Ehrlich, D.; Dillmann, B.; Ventrice, C., Jr.; Al Shamery, K.; Kuhlenbeck, H.; Freund, H.-J. Hydroxyl Groups on Oxide Surfaces: NiO (100), NiO (111), and Cr_2O_3 (111). *Chem. Phys.* **1993**, *177*, 533−546.
(40) McCafferty, E.; Wightman, J. P. Determination of the Concentration of Surface Hydroxyl Groups on Metal Oxide Films by a Quantitative XPS Method. *Surf. Interface Anal.* **1998**, *26*, 549−564.
(41) Zhou, G.; Wang, D.-W.; Yin, L.-C.; Li, N.; Li, F.; Cheng, H.-M. Oxygen Bridges between NiO Nanosheets and Graphene for Improvement of Lithium Storage. *ACS Nano* **2012**, *6* (4), 3214−3223.
(42) Natu, G.; Hasin, P.; Huang, Z.; Ji, Z.; He, M.; Wu, Y. Valence Band-Edge Engineering of Nickel Oxide Nanoparticles via Cobalt Doping for Application in *p*-Type Dye-Sensitized Solar Cells. *ACS Appl. Mater. Interfaces* **2012**, *4*, 5922−5929.
(43) Boschloo, G.; Hagfeldt, A. Spectroelectrochemistry of Nanostructured NiO. *J. Phys. Chem. B* **2001**, *105*, 3039−3044.
(44) Paulose, M.; Shankar, K.; Yoriya, S.; Prakasam, H. E.; Varghese, O. K.; Mor, G. K.; Latempa, T. A.; Fitzgerald, A.; Grimes, C. A. Anodic Growth of Highly Ordered TiO_2 Nanotube Arrays to 134 μm in Length. *J. Phys. Chem. B* **2006**, *110*, 16179−16184.
(45) Joshi, U. A.; Maggard, P. A. $CuNb_3O_8$: A *p*-Type Semiconducting Metal Oxide Photoelectrode. *J. Phys. Chem. Lett.* **2012**, *3*, 1577−1581.
(46) He, J. J.; Lindstrom, H.; Hagfeldt, A.; Lindquist, S. E. Dye-Sensitized Nanostructured Tandem Cell-First Demonstrated Cell with a Dye-Sensitized Photocathode. *Sol. Energy Mater. Sol. Cells* **2000**, *62*, 265−273.
(47) Irwin, M. D.; Buchholz, D. B.; Hains, A. W.; Chang, R. P. H.; Marks, T. J. *p*-Type Semiconducting Nickel Oxide as an Efficiency-Enhancing Anode Interfacial Layer in Polymer Bulk-Heterojunction Solar Cells. *Proc. Natl. Acad. Sci. U.S.A.* **2008**, *105*, 2783−2787.
(48) Teoh, W. Y.; Scott, J. A.; Amal, R. Progress in Heterogeneous Photocatalysis: From Classical Radical Chemistry to Engineering Nanomaterials and Solar Reactors. *J. Phys. Chem. Lett.* **2012**, *3*, 629−639.
(49) Kho, Y. K.; Teoh, W. Y.; Iwase, A.; Mädler, L.; Kudo, A.; Amal, R. Flame Preparation of Visible-Light-Responsive $BiVO_4$ Oxygen Evolution Photocatalysts with Subsequent Activation via Aqueous Route. *ACS Appl. Mater. Interfaces* **2011**, *3*, 1997−2004.
(50) Sun, Y.; Yan, K. P.; Wang, G. X.; Guo, W.; Ma, T. L. Effect of Annealing Temperature on the Hydrogen Production of TiO_2 Nanotube Arrays in a Two-Compartment Photoelectrochemical Cell. *J. Phys. Chem. C* **2011**, *115*, 12844−12849.
(51) Ng, C.; Ng, Y. H.; Iwase, A.; Amal, R. Influence of Annealing Temperature of WO_3 in Photoelectrochemical Conversion and Energy Storage for Water Splitting. *ACS Appl. Mater. Interfaces* **2013**, *5*, 5269−5275.
(52) Palomares, E.; Clifford, J. N.; Haque, S. A.; Lutz, T.; Durrant, J. R. Slow Charge Recombination in Dye-Sensitised Solar Cells (DSSC) Using Al_2O_3 Coated Nanoporous TiO_2 Films. *Chem. Commun.* **2002**, 1464−1465.
(53) Kim, E. S.; Nishimura, N.; Magesh, G.; Kim, J. Y.; Jang, J.-W.; Jun, H.; Kubota, J.; Domen, K.; Lee, J. S. Fabrication of $CaFe_2O_4$/TaON Heterojunction Photoanode for Photoelectrochemical Water Oxidation. *J. Am. Chem. Soc.* **2013**, *135*, 5375−5383.
(54) Bian, Z.; Tachikawa, T.; Cui, S.-C.; Fujitsuka, M.; Majima, T. Single-Molecule Charge Transfer Dynamics in Dye-Sensitized *p*-Type NiO Solar Cells: Influences of Insulating Al_2O_3 Layers. *Chem. Sci.* **2012**, *3*, 370−379.
(55) Park, J. H.; Kim, S.; Bard, A. J. Novel Carbon-Doped TiO_2 Nanotube Arrays with High Aspect Ratios for Efficient Solar Water Splitting. *Nano Lett.* **2006**, *6*, 24−28.
(56) Odobel, F.; Le Pleux, L.; Pellegrin, Y.; Blart, E. New Photovoltaic Devices Based on the Sensitization of *p*-Type Semiconductors: Challenges and Opportunities. *Acc. Chem. Res.* **2010**, *43*, 1063−1071.